



Exploring the Radio Spectral Energy Distribution of the Ultraluminous Radio-quiet Quasar SDSS J0100+2802 at Redshift 6.3

Yuanqi Liu^{1,2}, Ran Wang², Emmanuel Momjian³, Jeff Wagg⁴, Xiaolong Yang⁵, Tao An⁵, Yali Shao⁶, Chris L. Carilli^{3,7}, Xue-Bing Wu^{1,2}, Xiaohui Fan⁸, Fabian Walter^{3,9}, Linhua Jiang^{1,2}, Qiong Li^{1,2}, Jianan Li^{2,10}, Qinyue Fei^{1,2}, and Fuxiang Xu^{1,2}

¹ Department of Astronomy, School of Physics, Peking University, Beijing 100871, People's Republic of China

² Kavli Institute for Astronomy and Astrophysics, Peking University, Beijing 100871, People's Republic of China; rwangkia@pku.edu.cn

³ National Radio Astronomy Observatory, P.O. Box O, Socorro, NM 87801, USA

⁴ SKA Observatory, Lower Withington Macclesfield, Cheshire SK11 9FT, UK

⁵ Shanghai Astronomical Observatory, Key Laboratory of Radio Astronomy, CAS, 80 Nandan Road, Shanghai 200030, People's Republic of China

⁶ Max-Planck-Institut für Radioastronomie, Auf dem Hügel 69, D-53121 Bonn, Germany

⁷ Cavendish Laboratory, University of Cambridge, 19 J.J. Thomson Avenue, Cambridge CB3 0HE, UK

⁸ Steward Observatory, University of Arizona, 933 North Cherry Avenue, Tucson, AZ 85721, USA

⁹ Max Planck Institute for Astronomy, Königstuhl 17, D-69117 Heidelberg, Germany

¹⁰ Department of Astronomy, Tsinghua University, Beijing 100084, People's Republic of China

Received 2021 October 7; revised 2022 February 28; accepted 2022 March 5; published 2022 April 13

Abstract

We report deep Karl G. Jansky Very Large Array (VLA) observations of the optically ultraluminous and radio-quiet quasar SDSS J010013.02+280225.8 (hereafter J0100+2802) at redshift $z = 6.3$. We detected the radio continuum emission at 1.5 GHz, 6 GHz, and 10 GHz. This leads to a radio power-law spectral index of $\alpha = -0.52 \pm 0.18$ ($S \propto \nu^\alpha$). The radio source is unresolved in all VLA bands with an upper limit to the size of 0''.2 (i.e., ~ 1.1 kpc) at 10 GHz. We find variability in the flux density (increase by $\sim 33\%$) and the spectral index (steepened) between observations in 2016 and 2017. We also find that the VLA 1.5 GHz flux density observed in the same year is 1.5 times that detected with the Very Long Baseline Array (VLBA) in 2016 at the same frequency. This difference suggests that half of the radio emission from J0100+2802 comes from a compact core within 40 pc, and the rest comes from the surrounding few-kiloparsec area, which is diffuse and resolved out in the VLBA observations. The diffuse emission is 4 times brighter than what would be expected if driven by star formation. We conclude that the central active galactic nucleus is the dominant power engine of the radio emission in J0100+2802.

Unified Astronomy Thesaurus concepts: [Quasars \(1319\)](#); [Radio continuum emission \(1340\)](#); [Galaxies \(573\)](#); [High-redshift galaxies \(734\)](#)

1. Introduction

Quasars at $z \geq 6$ can serve as special laboratories to explore the formation and evolution of the first supermassive black holes (SMBHs), which formed at the end of cosmic reionization (Fan et al. 2006; Mazzucchelli et al. 2017). There are more than 200 quasars discovered at $z \geq 6$ (e.g., Willott et al. 2005, 2010; Jiang et al. 2009; Venemans et al. 2015; Matsuoka et al. 2016). SDSS J010013.02+280225.8 (hereafter J0100+2802) at $z = 6.327$, discovered by Wu et al. (2015), has a bolometric luminosity of $4.29 \times 10^{14} L_\odot$ and hosts a SMBH with an estimated mass of $1.3 \times 10^{10} M_\odot$. This quasar is the highest-redshift object among the optically ultraluminous quasars with $M_{1450} \leq -29$ known to date (Onken et al. 2020; Schindler et al. 2021). With detected X-ray emission from XMM–Newton (0.2–10 keV) and Chandra (2–10 keV) observations, J0100+2802 follows the $\alpha_{\text{OX}} - L_{2500\text{\AA}}$ relation of quasars with comparable ultraviolet luminosity at low to median ($1 < z < 5$) redshifts (Ai et al. 2017). The dust continuum, [C II], and CO emission lines have been mapped with multiband Atacama Large Millimeter/submillimeter Array (ALMA) observations at subkiloparsec-scale resolution

(Wang et al. 2019). The far-infrared (FIR) dust continuum indicates a nuclear star formation rate (SFR) of $1900 M_\odot \text{ yr}^{-1}$, while high- J CO line emission is detected as evidence of active galactic nucleus (AGN) contribution to heating the gas and dust in its host galaxy. Therefore, J0100+2802 provides a unique chance to study the early growth and nuclear activities of the most massive SMBHs in the epoch of cosmic reionization.

J0100+2802 is categorized as a radio-quiet quasar, with the definition of radio loudness $R < 10$, where the radio loudness is defined as the ratio of the rest-frame 5 GHz (radio) to the 4400 Å(optical) flux densities $R = S_{5 \text{ GHz}} / S_{4400 \text{ \AA}}$ (Kellermann et al. 1989). However, it is not silent, with an observed flux density of $104.5 \pm 3.1 \mu\text{Jy}$ at 3 GHz (Wang et al. 2016). Although radio-quiet quasars account for $\sim 90\%$ of the optically selected quasars (Ivezić et al. 2002; Bañados et al. 2015; Kellermann et al. 2016; Liu et al. 2021), their radio emission properties are not well studied at the highest redshift due to limited sensitivity. Therefore, little is known about their radio spectral index and emission mechanisms. The current observational studies of high-redshift quasars are concentrated on radio-loud ones, especially blazars (e.g., Zhang et al. 2017, 2020; An et al. 2020).

Only a compact core with a flux density lower than expected is detected with the Very Long Baseline Array (VLBA) at milliarcsecond (mas) resolution at 1.5 GHz (Wang et al. 2017). Measuring the radio spectral energy distribution (SED) with the



Original content from this work may be used under the terms of the [Creative Commons Attribution 4.0 licence](#). Any further distribution of this work must maintain attribution to the author(s) and the title of the work, journal citation and DOI.

VLA at arcsec resolution would help to determine if the radio spectrum is indeed flattened at low frequency, or if there is undetected radio emission on a large (kiloparsec) scale, which is crucial to explore the origins of the radio emission.

In this work, we carry out VLA observations of J0100+2802 at 1.5, 6, and 10 GHz and derive a power-law spectral index. This paper is organized as follows: the new radio observations and data reduction are described in Section 2. The observational results and analysis are shown in Section 3. We discuss the missing emission and possible origins in Section 4. The main conclusions are briefly summarized in Section 5.

We adopt a Λ CDM with $H_0 = 70 \text{ km s}^{-1} \text{ Mpc}^{-1}$, $\Omega_m = 0.3$, and $\Omega_\Lambda = 0.7$. With this cosmological model, 1'' at the redshift of J0100+2802 ($z = 6.3$) corresponds to 5.5 kpc. Throughout the article, we model the rest-frame radio continuum emission with a power law of $S_\nu \propto \nu^\alpha$, where S_ν is the flux density at frequency ν and α is the spectral index. All the frequencies mentioned are in the observed frame, unless noted otherwise.

2. Observations and Data Reduction

We observed the radio continuum emission from J0100+2802 using the VLA in the L , C , and X bands, spending a total of 4 hr in September and November 2017 in B configuration. The observations employ phase-referencing as our target is faint. The L -band observations use the 8-bit samplers, while C - and X -band observations use the 3-bit samplers.

Data reduction was performed with the Common Astronomy Software Applications package (CASA) version 5.6.3 (McMullin et al. 2007) using the standard VLA calibration pipeline. Data affected by radio frequency interference (RFI) were removed, and the imaging was performed using Briggs weighting with a robust parameter of 0.5. The flux density calibration accuracy is about 5% in all three bands. Self-calibration cannot improve the images because the target is not strong enough. The observation parameters and results are summarized in Table 1.

J0100+2802 was also observed at 1.5 GHz (L band) and 5 GHz (C band) in 2016 (program 16A-242), and the results are published in Sbarrato et al. (2021). The L -band observations in 2016 were carried out in B configuration, and the C -band observations in C configuration. We recalibrated and reimaged the data from this program with the same procedure as described above for the 2017 VLA observations. We also collect the observations from other VLA frequencies and VLBA (Wang et al. 2016, 2017), and low-frequency data from LOFAR (Gloudemans et al. 2021). These results are summarized in Table 1. We compare these measurements in Section 3.2.

3. Results and Analysis

3.1. Radio Emission and Spectral Index

Quasar J0100+2802 is detected in all three bands with a signal-to-noise ratio (S/N) larger than 10. The total intensity maps are shown in Figure 1. The source is unresolved in all three bands; hence we simply use the peak surface brightness in each band as the representative value of the continuum flux density. We adopt the uncertainty in the flux density measurement from the rms noise in the image because calibration errors are negligible in comparison. The continuum flux densities at 1.5 GHz, 6 GHz, and 10 GHz are $181 \pm 16 \mu\text{Jy}$, $82 \pm 4 \mu\text{Jy}$,

Table 1
New and Archive Radio Deep Observations of J0100+2802

	<i>L</i> band	<i>C</i> band	<i>X</i> band
Observing frequency range (GHz)	1.0–2.0	4.0–8.0	8.0–12.0
Observing central frequency (GHz)	1.5	6.0	10.0
Date of observations (in 2017)	1st Nov	16th Sep	07th Sep
Total on-source time (minutes)	100	40	40
Phase calibrator	J0119+3210	J0057+3021	J0057+3021
Flux/Bandpass calibrator	3C48	3C48	3C48
FWHM beam size* (")	5.8×3.8	1.7×1.1	1.0×0.6
Beam P.A. (°)	68.3	−73.4	−70.0
Image 1σ rms sensitivity ($\mu\text{Jy beam}^{-1}$)	16	4	4
Peak flux density ($\mu\text{Jy beam}^{-1}$)	181	82	55
Flux density of tapered image (μJy)		86 ± 7	69 ± 7
VLBA observations in 2016:			
Date of observations	Feb–Mar		
Total flux density (μJy)	88 ± 19		
VLA observations in 2016:			
Observing frequency range (GHz)	1.0–2.0	4.5–6.5	
Observing central frequency (GHz)	1.5	5.5	
Date of observations	May–Aug	Jan	
FWHM beam size* (")	4.6×3.6	4.9×3.7	
Flux density (μJy)	136 ± 10	104 ± 5	

Note. Using robust weighting for observations both in 2016 and in 2017.

and $55 \pm 4 \mu\text{Jy}$, respectively (Table 1). The positions of the radio center and optical center from the Sloan Digital Sky Survey (SDSS) catalog are consistent within the uncertainties of the astrometry accuracy of SDSS.

To compare the flux densities at the same scale, we tapered the visibility data of the 6 and 10 GHz observations to a similar resolution of the 1.5 GHz image. There are no significant differences ($>2\sigma$) in flux density between full-resolution images and tapered images at both 6 and 10 GHz. We will adopt the results of the tapered images at 6 and 10 GHz with the same resolution as the 1.5 GHz image for the analysis that follows. These values are listed in Table 1.

We fit a power law to the radio continuum using the VLA measurements at 1.5, 6, and 10 GHz. We derive the spectral index by applying the MCMC algorithm with the Python package emcee (Foreman-Mackey et al. 2013). The 100 models in parameter space (gray) and best-fitting result of the spectral index (red) are shown in Figure 2. The continuum flux densities are shown as blue circles. The radio emission measured with the VLA can be well fitted by a single power law with a spectral index of $\alpha = -0.52 \pm 0.18$. There is no sign of flattening or turnover in the rest-frame frequency range of 7 to 84 GHz.

A mean spectral index of $\alpha \sim -0.5$ is reported from multiple investigations using large radio-quiet quasar samples at low to medium redshift ($0 < z < 3$; e.g., Barvainis et al. 1996; Kukula et al. 1998; Gim et al. 2019; Zajaček et al. 2019). The spectral index of $\alpha = -0.52 \pm 0.18$ found in J0100+2802 is within the

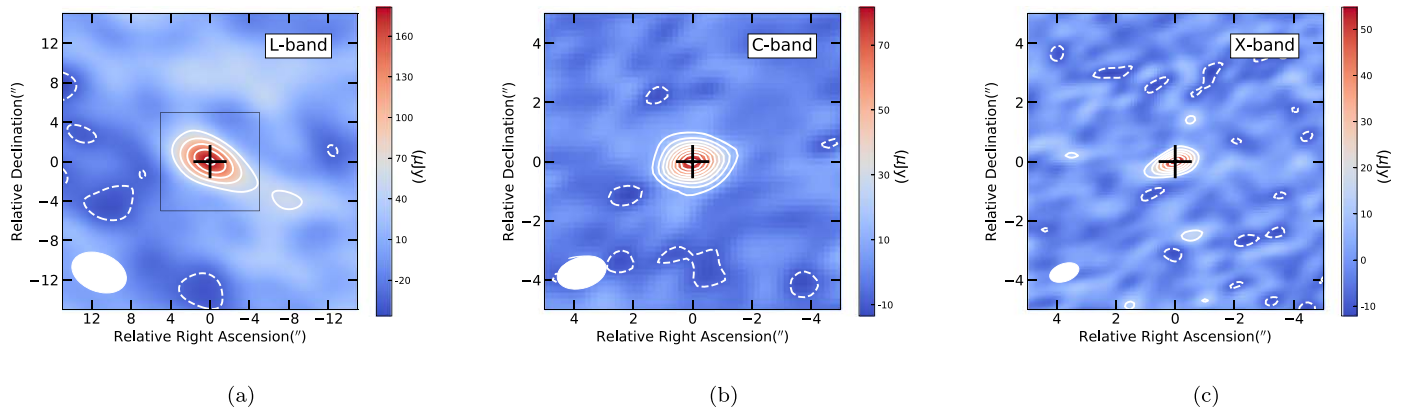


Figure 1. J0100+2802 images at (a) 1.5 GHz, (b) 6 GHz and (c) 10 GHz VLA observations. The contour levels are at $(-2, 3, 5, 7, \dots, 19)$ times the corresponding 1σ rms noise level of each image (see Table 1). Black crosses denote the optical position (R.A. = $01^{\text{h}}00^{\text{m}}13^{\text{s}}027$, decl. = $+28^{\circ}02'25.^{\prime\prime}80$). Synthesized beams are shown as the ellipses at the bottom left. The box in panel (a) shows the image size of panels (b) and (c).

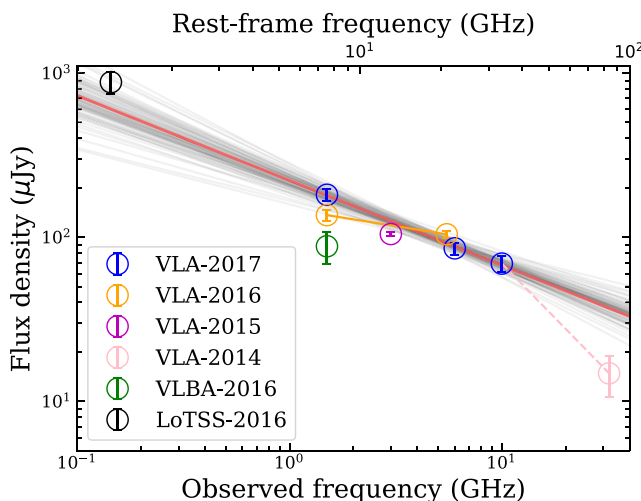


Figure 2. Radio continuum of J0100+2802 at observing frequencies of 1.5 to 32 GHz at different epochs. The new VLA observations at 1.5 GHz, 6 GHz, and 10 GHz in 2017 are shown as blue circles, which (with their error bars) are used in fitting the power-law model by the MCMC algorithm. Their errors contain only map rms and not calibration errors. Gray lines represent 100 sets of models that are randomly selected from the parameter space, which visualize the uncertainties. The red line denotes the best-fitting result with a spectral index of $\alpha = -0.52 \pm 0.18$. For comparison, the orange circles refer to VLA 1.5 GHz and 5 GHz flux densities observed in 2016 (program 16A-242), which indicate a two-point spectra of $\alpha_{2016} = -0.21 \pm 0.10$. The green circle shows the flux density from the VLBA 1.5 GHz observations in 2016 (Wang et al. 2017), the magenta circle represents the VLA 3 GHz in 2015, and the pink circle represents the 32 GHz flux density in 2014 (Wang et al. 2016). The pink dashed line shows a possible steeper spectra fitted from X-band and Ka-band observations.

range of spectral indices in low- z radio-quiet quasars. This suggests common radio emission origins and mechanisms, e.g., synchrotron emission powered by AGN (Bridle & Perley 1984; Laing & Bridle 2013) and/or nuclear star-forming activity (Condon 1992; Condon et al. 2013). We will further discuss the radio emission mechanism in Section 4.2.

With the derived spectral index, we estimate the radio loudness (R) of J0100+2802 to be $R = 0.6$, confirming the result in Wang et al. (2016) that the source is radio-quiet (i.e., $R \leq 10$; Kellermann et al. 1989; Sikora et al. 2007).

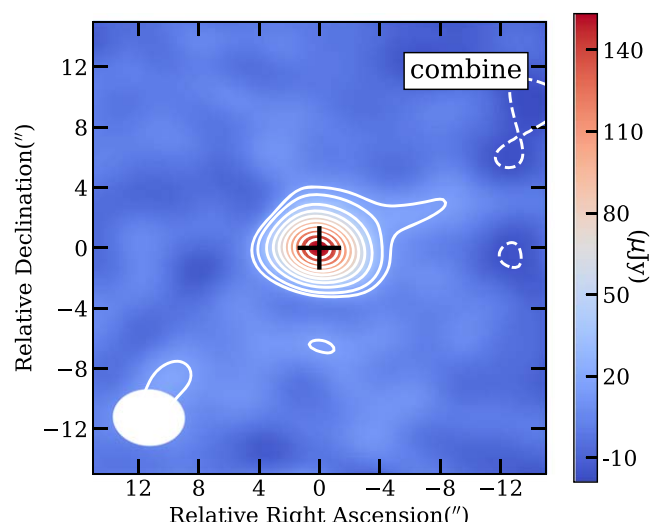


Figure 3. J0100+2802 images combining the observations of 2016 and 2017 at 1.5 GHz. The contour levels are at $(-2, 2, 3, 5, 7, \dots, 19)$ times the corresponding 1σ rms noise level of $7 \mu\text{Jy}/\text{beam}$. The synthesis beam is shown as the left bottom ellipse with a FWHM size of $4''/6 \times 3''/6$.

3.2. Comparison with Radio Continuum from Other Epochs

The VLA observations in 2016 show an unresolved source with peak flux density of $136.2 \pm 10.4 \mu\text{Jy}$ with a beam size of $4.^{\prime\prime}6 \times 3.^{\prime\prime}6$ at 1.5 GHz and a flux density of $104.1 \pm 5.4 \mu\text{Jy}$ with a beam size of $4.^{\prime\prime}9 \times 3.^{\prime\prime}7$ at 5.5 GHz. The fit to the data in 2016 yields a power-law spectral index of $\alpha_{2016} = -0.21 \pm 0.10$. We note that the *L*-band measurement we obtained is slightly lower than the value of $154 \pm 12 \mu\text{Jy}$ published in Sbarrato et al. (2021), but is still marginally consistent considering the uncertainties. This is likely to be due to the difference in calibration and imaging methods. Although a tentative jet is reported in Sbarrato et al. (2021), there is no sign of extended structures with $S/N > 3$ in our 1.5 GHz and 6 GHz images. Combining the data from 2016 and 2017 to achieve better sensitivity, no signal of jet emission is detected at $\leqslant 3\sigma$ in the image as shown in Figure 3.

The deep VLA *S*-band (3 GHz) and *Ka*-band (32 GHz) observations of this source were reported in Wang et al. (2016), with continuum flux densities of $S_{\text{3 GHz}} = 104.5 \pm 3.1 \mu\text{Jy}$ and $S_{\text{32 GHz}} = 14.8 \pm 4.3 \mu\text{Jy}$, respectively. These two detections are shown as magenta circles in Figure 2. The flux density

measured at 3 GHz is consistent with both the power-law spectra fitted from observations in 2017 and those in 2016. As shown in the figure, the 32 GHz flux density does not fit this single power-law well. Thermal emission may also contribute to the flux density at such high frequency in the source rest frame, so the current detection should be the upper limit of radio activity. This may suggest a steeper spectral index of $\alpha = -1.32 \pm 0.31$ at higher frequencies, i.e., at rest frame >100 GHz to 234 GHz. However, the observed-frame 32 GHz continuum flux density has large uncertainties due to the low S/N (~ 3). Quasar J0100+2802 was also detected in the Low Frequency Array (LOFAR) Two Meter Sky survey (LoTSS) data release 2 (DR2; Shimwell et al. 2022), which was published very recently (Gloudemans et al. 2021). The LoTSS data were taken in October 2016 at 144 MHz with a point-source flux density of $S_{144\text{ MHz}} = 0.88 \pm 0.13 \mu\text{Jy}$. The LOFAR measurement combined with the VLA L -band data in 2017 reveal a steep spectral index of $\alpha_{\text{low1}} = 0.67 \pm 0.10$ or $\alpha_{\text{low2}} = 0.80 \pm 0.10$ using the 2016 data, which suggest that the radio spectrum is getting steeper toward lower frequencies.

The VLBA observations in 2016 of J0100+2802 show a compact core with no extended structures. The intrinsic brightness temperature is estimated to be $T_B = (1.6 \pm 1.2) \times 10^7 \text{ K}$, which is higher than the typical value of normal galaxies ($\leq 10^5 \text{ K}$; Condon 1992). Thus, the VLBA emission likely is due to nonthermal synchrotron emission driven by AGN activity rather than a star formation origin, such as from compact H II regions, radio SNe, or compact SN remnants (see Maini et al. 2016 for more details).

4. Discussion

4.1. Variability and the Missing Emission

A comparison of the VLA measurements in 2016 and 2017 suggests possible variability in both the radio flux densities and spectral index. The flux density at 1.5 GHz is increased by $45.1 \pm 19.2 \mu\text{Jy}$ (33% of the total flux in 2016) in a time period of 15 months in the observed frame. This period corresponds to two months in the rest frame. Meanwhile, the radio emission is marginally decreased at 5 GHz by $9.7 \pm 9.5 \mu\text{Jy}$, deriving the 5 GHz flux density in 2017 with the fitted spectral index. Thus, the spectral index fitted between these two bands has steepened from $\alpha_{2016} = -0.21 \pm 0.10$ to $\alpha_{2017} = -0.54 \pm 0.13$.

The VLBA observations were carried out in 2016 February and March, which is four months in the observed frame on average before the VLA 1.5 GHz observations in 2016 May to August. We find a 1.5 GHz flux density difference of $48.2 \pm 21.6 \mu\text{Jy}$ (35% of the total flux detected by VLA in 2016) between the VLA and VLBA observations. This may also be understood as an increase in the radio emission as was suggested by the two-epoch VLA observations at 1.5 GHz. However, we note that the VLBA measurement is lower than the flux density extrapolated from the 3 GHz data observed in 2015 as well (Wang et al. 2016). Thus, in addition to radio variability, radio emission on different scales also needs to be seriously considered to explain the difference in flux density between the VLA and VLBA flux densities.

4.2. Emission on Different Scales

The minimum resolvable size in our VLA observations is $1''.1$, which is estimated from $\theta = b_\phi \sqrt{\frac{4 \ln 2}{\pi} \ln \left(\frac{\text{SNR}}{\text{SNR} - 1} \right)}$, with

beam size $b_\phi = \sqrt{b_{\max} \times b_{\min}} = 4''.1$ (Kovalev et al. 2005). This angular size corresponds to 6.1 kpc at the redshift of J0100+2802. Adopting the same formula, we obtain the minimum resolvable size of VLA 6 GHz and 10 GHz observations in 2017, which are 1.6 kpc and 1.1 kpc, respectively. As the source flux densities in the tapered images only marginally increased within the uncertainties ($< 1\sigma$ in 6 GHz, 2σ in 10 GHz results), we consider the radio emission detected in these three bands to be from the same region. This implies that the size of the radio source detected in our VLA observation is on a scale of $\lesssim 1.1$ kpc.

The VLBA mas-scale resolution imaging of the central region yields a source size of $(40 \pm 20) \times (18 \pm 10)$ pc and a flux density of $88.0 \pm 19.0 \mu\text{Jy}$ (Wang et al. 2017).

The radio flux that is missed by the VLBA observation is likely to arise from the central kiloparsec region and that is unresolved by the VLA. Such a component could be too extended to be detected by the VLBA (e.g., a few hundreds parsec to 1 kpc) and/or consist of several radio knots with surface brightness below the VLBA detection limit.

The missing radio flux density problem was widely reported with mas-resolution imaging of samples of radio-quiet quasars, while the origins of such diffuse emission are rarely discussed. For the radio-quiet Palomar-Green (PG) quasars with VLA observations, a certain percentage of them would be detected by VLBI observations with a lower flux densities (e.g., 8/12; Blundell & Beasley 1998, 9/16, A. Wang 2022, in preparation). For moderate redshift ($1 < z < 2$) radio-quiet quasars, around $50\% \sim 75\%$ flux densities are recovered by VLBI observations (Herrera Ruiz et al. 2016; Maini et al. 2016). Not only radio-quiet quasars, but also radio-loud quasars and other types of sources can show missing flux on VLBI scales (e.g., the radio-loudest quasar at redshift 6, Momjian et al. 2018; four hot dust-obscured galaxies Frey et al. 2016).

In radio-quiet quasars, the origins of the radio emission can be both star formation and AGN activity, such as weak jets, winds, and free-free emission from the corona (White et al. 2017; Panessa et al. 2019). For example, high-resolution VLBI observations reveal a prominent jet and multiple-phase outflows in Mrk 231, which is the closest ($z = 0.042$) radio-quiet AGN (Neff & Ulvestad 1988; Ulvestad et al. 1999a, 1999b; Wang et al. 2021). Therefore, the missing radio emission of J0100+2802 can be powered by star formation in the surrounding area, or the central engine, or a combination of both. We discuss the possible origins in the following sections.

4.2.1. Emission from Star Formation

First, we assume that all the radio emission, which is undetected at 1.5 GHz by the VLBA, originates from star formation. The corresponding SFR is estimated to be $7900 M_\odot \text{ yr}^{-1}$, according to the relation in Murphy et al. (2011):

$$\left(\frac{\text{SFR}_{1.4 \text{ GHz}}}{M_\odot \text{ yr}^{-1}} \right) = 6.35 \times 10^{-29} \left(\frac{L_{1.4 \text{ GHz}}}{\text{erg s}^{-1} \text{ Hz}^{-1}} \right), \quad (1)$$

which is based on the FIR-radio correlation of IR-luminous star-forming galaxies (Yun et al. 2001). Here we use a typical radio spectral index of $\alpha = -0.7$ for star-forming galaxies to derive the luminosity $L_{1.4 \text{ GHz}}$ at rest-frame 1.4 GHz (Condon et al. 2013). If we assume a nuclear SFR of $1900 M_\odot \text{ yr}^{-1}$ (Wang et al. 2019) in the central kiloparsec region, based on

Equation (1), the rest-frame 1.4 GHz radio luminosity associated with the star-forming activity is $L_{1.4 \text{ GHz}} = 1.1 \times 10^7 L_\odot$. Note that the dust-continuum-based SFR should be considered as an upper limit as AGN activity could contribute to the dust heating. Adopting the same radio spectral index of $\alpha = -0.7$, this corresponds to a flux density of $11.6 \mu\text{Jy}$ at 1.4 GHz in the observing frame. This accounts for only around 1/4 of the VLA radio flux density not detected by the VLBA. Therefore, nuclear star formation is unlikely to be the dominant source of the radio emission on kiloparsec scales.

4.2.2. Emission from AGN Activity

AGN outflows on >100 pc to the kiloparsec scale, including uncollimated winds or low-surface brightness collimated jets, could be a possible source of the radio emission in radio-quiet quasars (Panessa et al. 2019).

Radio emission originating from winds has been reported in Hwang et al. (2018) with a sample of radio-quiet quasars at $z = 2 - 3$. Winds driven by AGNs are normally identified by narrow-line kinematics, for instance, the blueshifted [O III] emission line (Christopoulou et al. 1997; Zakamska & Greene 2014; Zakamska et al. 2016). The evidence of AGN-powered outflow in J0100+2802 is ambiguous. The quasar's broad MgII emission is blueshifted by $1020 \pm 250 \text{ km s}^{-1}$ compared to the [C II] and CO redshift of the quasar host galaxy, suggesting outflowing gas in the broad-line region. However, there is no evidence of kiloparsec-scale outflows based on the ALMA observations of [C II] and CO lines in the central kiloparsec region of the quasar host galaxy in 2016 (Wang et al. 2019). The narrow-line kinematics are impossible to measure for quasar J0100+2802. The wind can be inferred from the high optical luminosity, which is sufficient to produce synchrotron emission from shock accelerated relativistic electrons ($\nu L_\nu \sim 10^{-5} L_{\text{AGN}}$, where L_{AGN} is the AGN bolometric luminosity; Ishibashi & Courvoisier 2011; Nims et al. 2015).

Weak, low-surface brightness jets driven by AGN can be another possible origin of the missing radio emission in radio-quiet quasars. Strong jets are highly collimated, while less powerful jets may have a lower efficiency of collimating the flow (Falcke & Biermann 1995; Panessa et al. 2019).

In the recent study of the hyperluminous, dust-obscured, and radio-quiet quasar W2246-0526 at redshift $z = 4.6$ (Fan et al. 2020), the authors also discuss the AGN-driven origins of the missing radio emission. VLBI observations resolve a compact core of flux density $75 \pm 9 \mu\text{Jy}$, which only accounts for 10% of the total flux density observed with the VLA at the same frequency. Similar to J0100+2802, the flux density difference represents low-brightness diffuse emission at ≥ 32 pc (VLBI-observed component size) to the kiloparsec scale. They consider such VLBI-undetected radio emission as being associated with pc-scale winds and/or a low-power jet. The VLBA-undetected radio emission of J0100+2802 may have a similar origin.

4.3. Overview of the Missing Emission

We consider that both time variability and emission from different scales may contribute to the discrepant flux density between the VLA and VLBA measurements at 1.5 GHz. While the compact radio core emission detected by both VLA and VLBA is likely to be dominated by the central luminous AGN

(Wang et al. 2017; Sbarrato et al. 2021), the radio emission at a larger scale may be from a more diffuse component powered by an AGN wind and/ or low-surface brightness knots of weak jets. Nuclear star-forming activity could also contribute to the diffuse radio emission on the kiloparsec scale.

J0100+2802 is an example to show the missing emission in radio-quiet quasars at $z > 6$. It provides a new window to explore the origin and mechanisms of radio emission at different scales. The related AGN-driven wind shocks and the low-power jet are considered to provide a feedback mode in radio-quiet quasars (King & Pounds 2015; Ishibashi et al. 2021). High-sensitivity VLA and VLBI observations of a larger sample are needed, to better constrain the percentage of missing emission and understand the mechanisms. The radio variability in J0100+2802 should also be confirmed with additional VLA and VLBA observations.

5. Conclusion

From studies of quasars in the universe, we now know that the radio-quiet sources should be the most abundant population. However, at the highest redshifts, this faint population could not be studied in detail due to the limits of observational sensitivity. J0100+2802 is a particular optically luminous and radio-quiet quasar at $z \geq 6$, which has been detected with both high-resolution VLBA observations and a relatively complete radio SED covering from the rest-frame frequency range 7 to 234 GHz.

In this paper, we report the radio spectral index to be $\alpha = -0.52 \pm 0.18$ fitted from the multiwavelength radio continuum flux densities observed in 2017. We find a slight variability from 2016 to 2017, which possibly indicates AGN activity. We compare the VLA 1.5 GHz result with VLBA observations at the same frequency (Wang et al. 2017) to constrain the radio emission at different spatial scales. The compact core accounts for more than half of the emission, which is triggered by AGN activity. The missing emission is resolved on tens of parsec to kiloparsec scales. This diffuse emission may originate from star formation and AGN-driven outflow. Overall, we conclude that the radio emission is mainly due to AGN rather than star formation. J0100+2802 is currently an excellent example of a radio-quiet quasar at such high redshifts. However, the appearance of low-power jet and AGN wind on the kiloparsec scale are difficult to distinguish. Deep imaging in the radio at intermediate ($\sim 0.^{\prime\prime}1$) resolution filling the gap between VLA and VLBA resolutions will be critical to address this question.

To better understand the characteristics of radio SEDs of the most distant quasars, we require deeper and high-resolution observations of a complete sample of radio-quiet quasars. From research on spatial distribution of radio emission as well as other radio features (e.g., morphology, spectral index), the respective contribution of AGN and star formation activity will be better constrained. The missing radio emission may help better understand the AGN feedback and the evolution of SMBHs.

This work is supported by the National Key Program for Science and Technology Research and Development (grant 2016YFA0400703). We acknowledge support from the National Science Foundation of China (NSFC) grant Nos. 11991052, 11721303, 12173002, 11373008, and 11533001. X. L.Y. thanks the support by the Shanghai Sailing Programme

(21YF1455300) and the National Science Foundation of China (12103076). We thank Professor Gregory J. Herczeg, PhD student Lulu Zhang, and Yang Li in PKU for writing comments in this article. The National Radio Astronomy Observatory (NRAO) is a facility of the National Science Foundation operated under cooperative agreement by Associated Universities, Inc. This paper makes use of the VLA data from program 17B-071, 16A-242.

Facilities: VLA, CASA.

ORCID iDs

- Yuanqi Liu <https://orcid.org/0000-0001-9321-6000>
 Ran Wang <https://orcid.org/0000-0003-4956-5742>
 Emmanuel Momjian <https://orcid.org/0000-0003-3168-5922>
 Xiaolong Yang <https://orcid.org/0000-0002-4439-5580>
 Tao An <https://orcid.org/0000-0003-4341-0029>
 Yali Shao <https://orcid.org/0000-0002-1478-2598>
 Chris L. Carilli <https://orcid.org/0000-0001-6647-3861>
 Xue-Bing Wu <https://orcid.org/0000-0002-7350-6913>
 Xiaohui Fan <https://orcid.org/0000-0003-3310-0131>
 Fabian Walter <https://orcid.org/0000-0003-4793-7880>
 Linhua Jiang <https://orcid.org/0000-0003-4176-6486>
 Qiong Li <https://orcid.org/0000-0002-3119-9003>
 Jianan Li <https://orcid.org/0000-0002-1815-4839>

References

- Ai, Y., Fabian, A. C., Fan, X., et al. 2017, *MNRAS*, **470**, 1587
 An, T., Mohan, P., Zhang, Y., et al. 2020, *NatCo*, **11**, 143
 Bañados, E., Venemans, B. P., Morganson, E., et al. 2015, *ApJ*, **804**, 118
 Barvainis, R., Lonsdale, C., & Antonucci, R. 1996, *AJ*, **111**, 1431
 Blundell, K. M., & Beasley, A. J. 1998, *MNRAS*, **299**, 165
 Bridle, A. H., & Perley, R. A. 1984, *ARA&A*, **22**, 319
 Christopoulou, P. E., Holloway, A. J., Steffen, W., et al. 1997, *MNRAS*, **284**, 385
 Condon, J. J. 1992, *ARA&A*, **30**, 575
 Condon, J. J., Kellermann, K. I., Kimball, A. E., Ivezić, Ž., & Perley, R. A. 2013, *ApJ*, **768**, 37
 Falcke, H., & Biermann, P. L. 1995, *A&A*, **293**, 665
 Fan, L., Chen, W., An, T., et al. 2020, *ApJL*, **905**, L32
 Fan, X., Carilli, C. L., & Keating, B. 2006, *ARA&A*, **44**, 415
 Foreman-Mackey, D., Hogg, D. W., Lang, D., & Goodman, J. 2013, *PASP*, **125**, 306
 Frey, S., Paragi, Z., Gabányi, K. É., & An, T. 2016, *MNRAS*, **455**, 2058
 Gim, H. B., Yun, M. S., Owen, F. N., et al. 2019, *ApJ*, **875**, 80
 Gloudemans, A. J., Duncan, K. J., Röttgering, H. J. A., et al. 2021, *A&A*, **656**, A137
 Herrera Ruiz, N., Middelberg, E., Norris, R. P., & Maini, A. 2016, *A&A*, **589**, L2
 Hwang, H.-C., Zakamska, N. L., Alexander, R. M., et al. 2018, *MNRAS*, **477**, 830
 Ishibashi, W., & Courvoisier, T. J. L. 2011, *A&A*, **525**, A118
 Ishibashi, W., Fabian, A. C., & Arakawa, N. 2021, *MNRAS*, **502**, 3638
 Jiang, L., Fan, X., Bian, F., et al. 2009, *AJ*, **138**, 305
 Kellermann, K. I., Condon, J. J., Kimball, A. E., Perley, R. A., & Ivezić, Ž. 2016, *ApJ*, **831**, 168
 Kellermann, K. I., Sramek, R., Schmidt, M., Shaffer, D. B., & Green, R. 1989, *AJ*, **98**, 1195
 King, A., & Pounds, K. 2015, *ARA&A*, **53**, 115
 Kovalev, Y. Y., Kellermann, K. I., Lister, M. L., et al. 2005, *AJ*, **130**, 2473
 Kukula, M. J., Dunlop, J. S., Hughes, D. H., & Rawlings, S. 1998, *MNRAS*, **297**, 366
 Laing, R. A., & Bridle, A. H. 2013, *MNRAS*, **432**, 1114
 Liu, Y., Wang, R., Momjian, E., et al. 2021, *ApJ*, **908**, 124
 Maini, A., Prandoni, I., Norris, R. P., Giovannini, G., & Spitler, L. R. 2016, *A&A*, **589**, L3
 Matsuoka, Y., Onoue, M., Kashikawa, N., et al. 2016, *ApJ*, **828**, 26
 Mazzucchelli, C., Bañados, E., Venemans, B. P., et al. 2017, *ApJ*, **849**, 91
 McMullin, J. P., Waters, B., Schiebel, D., Young, W., & Golap, K. 2007, in *ASP Conf. Ser.* 376, *Astronomical Data Analysis Software and Systems XVI*, ed. R. A. Shaw, F. Hill, & D. J. Bell (San Francisco, CA: ASP), **127**
 Ivezić, Ž., Menou, K., Knapp, G. R., et al. 2002, *AJ*, **124**, 2364
 Momjian, E., Carilli, C. L., Bañados, E., Walter, F., & Venemans, B. P. 2018, *ApJ*, **861**, 86
 Murphy, E. J., Condon, J. J., Schinnerer, E., et al. 2011, *ApJ*, **737**, 67
 Neff, S. G., & Ulvestad, J. S. 1988, *AJ*, **96**, 841
 Nims, J., Quataert, E., & Faucher-Giguère, C.-A. 2015, *MNRAS*, **447**, 3612
 Onken, C. A., Bian, F., Fan, X., et al. 2020, *MNRAS*, **496**, 2309
 Panessa, F., Baldi, R. D., Laor, A., et al. 2019, *NatAs*, **3**, 387
 Sbarato, T., Ghisellini, G., Giovannini, G., & Giroletti, M. 2021, *A&A*, **655**, A95
 Schindler, J.-T., Fan, X., Novak, M., et al. 2021, *ApJ*, **906**, 12
 Shimwell, T. W., Hardcastle, M. J., Tasse, C., et al. 2022, *A&A*, **659**, A1
 Sikora, M., Stawarz, Ł., & Lasota, J.-P. 2007, *ApJ*, **658**, 815
 Ulvestad, J. S., Wrobel, J. M., & Carilli, C. L. 1999a, *ApJ*, **516**, 127
 Ulvestad, J. S., Wrobel, J. M., Roy, A. L., et al. 1999b, *ApJL*, **517**, L81
 Venemans, B. P., Bañados, E., Decarli, R., et al. 2015, *ApJL*, **801**, L11
 Wang, A., An, T., Jaiswal, S., et al. 2021, *MNRAS*, **504**, 3823
 Wang, F., Wang, R., Fan, X., et al. 2019, *ApJ*, **880**, 2
 Wang, R., Momjian, E., Carilli, C. L., et al. 2017, *ApJL*, **835**, L20
 Wang, R., Wu, X.-B., Neri, R., et al. 2016, *ApJ*, **830**, 53
 White, S. V., Jarvis, M. J., Kalfountzou, E., et al. 2017, *MNRAS*, **468**, 217
 Willott, C. J., Delfosse, X., Forveille, T., Delorme, P., & Gwyn, S. D. J. 2005, *ApJ*, **633**, 630
 Willott, C. J., Delorme, P., Reylé, C., et al. 2010, *AJ*, **139**, 906
 Wu, X.-B., Wang, F., Fan, X., et al. 2015, *Natur*, **518**, 512
 Yun, M. S., Reddy, N. A., & Condon, J. J. 2001, *ApJ*, **554**, 803
 Zajaček, M., Busch, G., Valencia-S., M., et al. 2019, *A&A*, **630**, A83
 Zakamska, N. L., & Greene, J. E. 2014, *MNRAS*, **442**, 784
 Zakamska, N. L., Hamann, F., Páris, I., et al. 2016, *MNRAS*, **459**, 3144
 Zhang, Y., An, T., Frey, S., et al. 2017, *MNRAS*, **468**, 69
 Zhang, Y., An, T., & Frey, S. 2020, *SciBu*, **65**, 525